ACS APPLIED ELECTRONIC MATERIALS

Open Access

This article is licensed under CC-BY 4.0

pubs.acs.org/acsaelm Article

Synthesis of Plasmonically Active Titanium Nitride Using a Metallic Alloy Buffer Layer Strategy

Arthur F. Lipinski,[§] Christopher W. Lambert,[§] Achyut Maity,*[,§] William R. Hendren, Paul R. Edwards, Robert W. Martin, and Robert M. Bowman*

Cite This: ACS Appl. Electron. Mater. 2023, 5, 6929–6937

Read Online

ACCESS | Metrics & More | Article Recommendations | Supporting Information

ABSTRACT: Titanium nitride (TiN) has emerged as a highly promising alternative to traditional plasmonic materials. This study focuses on the inclusion of a $Cr_{90}Ru_{10}$ buffer layer between the substrate and thin TiN film, which enables the use of cost-effective, amorphous technical substrates while preserving high film quality. We report best-in-class TiN thin films fabricated on fused silica wafers, achieving a maximum plasmonic figure of merit, $-\epsilon'/\epsilon''$, of approximately 2.8, even at a modest wafer temperature of around 300 °C. Furthermore, we delve into the characterization of TiN thin film quality and fabricated TiN triangular nanostructures, employing attenuated total reflectance and cathodoluminescence techniques to highlight their potential applications in surface plasmonics.

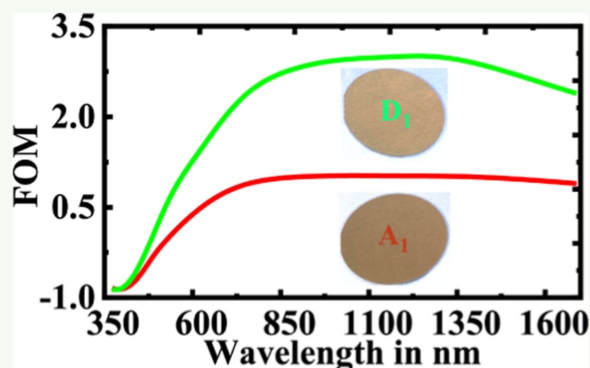

KEYWORDS: *thin film deposition, sputtering, alternative transition metal nitrides, titanium nitride (TiN), FOM, surface plasmon, ATR, Kretschmann−Reather (KR) configuration, plasmon coupling, single particle spectroscopy, cathodoluminescence (CL)*

■ INTRODUCTION

Transition metal nitride materials have garnered much recent interest because their plasmonic and refractory properties making them promising candidates for applications which require conditions such as mechanical robustness and high temperatures that limit the use of traditional plasmonic materials like gold or silver.[1] Recent studies have also demonstrated the surface plasmon-assisted optical response of the metallic TiN in the visible and infrared spectral ranges. The exceptional combination of thermal and chemical stability, which extends even to temperatures as high as 1400 °C, while concurrently exhibiting plasmonic activity,[2] underscores TiN as an extraordinarily promising candidate for a number of applications, including photothermal-based plasmonic applications, solar absorbers,[3−7] photothermal medical therapy,[8,9] and heat-assisted magnetic recording (HAMR) to name a few.[10] As such, studies have been undertaken to improve the optical properties of TiN to shift plasmonic quality even closer to that of gold.[11−20]

Highly metallic TiN films can be grown by several techniques, such as reactive sputtering, plasma-enhanced atomic layer deposition (PE-ALD),[21,22] pulsed laser deposition,[6,16,23] molecular-beam epitaxy,[18,24] and so forth.

It has been observed that magnetron sputtering provides the potential to deposit smooth and highly metallic TiN thin films, even below 10 nm.[17] These studies have mostly involved the use of substrates such as MgO and Al_2O_3 in order to achieve the best possible lattice matching, which encourages selective crystalline growth.[18,20,21,24−29] For quite some time, MgO has been the substrate of choice for growing highly textured/epitaxial TiN thin films to yield metallicity and improved optical properties. MgO substrates are comparatively expensive ($/cm^2), hygroscopic, and harder to integrate into the existing manufacturing processes.[30] Usually the fabrication process takes place at very high substrate temperatures, typically at 500°−600 °C or even higher, enabling the lattice matching between the TiN film and the substrate.[18,20,24,26−28] Though high-temperature depositions of TiN on expensive MgO and Al_2O_3 substrates have shown excellent performance, they are unlikely to be practical for use in industrial processes. Applications including silicon microelectronics or flexible electronics, especially in complementary metal-oxide-semiconductor technology, require a low ceiling temperature no higher than 500 °C.[31]

In order to qualify for practical or industrial realization, it is necessary to produce TiN within a reduced thermal budget (lower substrate temperatures and no post annealing) and

Received: September 25, 2023
Revised: December 1, 2023
Accepted: December 4, 2023
Published: December 13, 2023

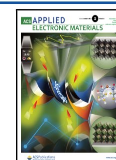

© 2023 The Authors. Published by American Chemical Society

include amorphous technical substrates, such as fused silica, which offers little in the way of orientated film growth. In this context, the use of an additional buffer layer might be an excellent alternative option to fabricate highly metallic TiN films with a high figure of merit (FOM) ($-\epsilon'/\epsilon''$, where ϵ' and ϵ'' are the real and imaginary part of the dielectric function, respectively) at relatively low temperature. For instance, in a study conducted by Ding et al.,[32] it was demonstrated that the use of a MgO buffer layer on a Si(001) substrate could improve the FOM of TiN produced through PE-ALD, even at a moderate substrate temperature of 450 °C. However, there is a preference for exploring simpler buffer layer options due to their potential attractiveness.

In this context, Cr[33] or Cr-alloy materials[34] can be an alternative solution owing to their strength and ductility at higher temperatures.[35] The use of a Cr as an adhesion/seed layer to deposit metal thin films has been a long-standing standard.[36,37] The compatibility of Cr materials is already well established[36−38] while the research on the compatibility of the Cr-alloys, such as $Cr_{90}Ru_{10}$, is currently very rare.[39] Although Dong et al.[39] have shown that the use of CrRu as an intermediate layer initiates the textured growth of TiN; however, the extensive optical properties of deposited TiN thin films using CrRu as a buffer/seed layer have not been studied so far. Beneficially CrRu does not introduce additional contamination through oxidation at higher temperature deposition.[40,41]

In this article, we have addressed the novel use of a chromium ruthenium ($Cr_{90}Ru_{10}$) alloy buffer layer to attain best-in-class FOM at wafer deposition temperatures ∼300 °C and demonstrated the plasmonic functionality in patterned nanoentities. The crystalline characteristics and thickness of the films were investigated by X-ray diffraction (XRD) and reflection techniques. The optical dielectric function of the TiN films was estimated through the experimentally acquired spectroscopic ellipsometry data. We demonstrate the excitation of the surface plasmon polariton (SPP), through its coupling with an evanescent wave of the incident light wave at the TiN/air interface with attenuated total reflection (ATR) using the Kretschmann−Raether configuration (KR configuration). The multilayer reflection model for stratified media was used to support the experimentally acquired data and to demonstrate the sensitivity of the coupling efficiency on mediums of differing refractive index, which may have potential use in the design of refractive index sensors and biosensors. We have also demonstrated the localized surface plasmon-assisted optical properties of a TiN triangular nano-object using hyperspectral cathodoluminescence (CL) imaging and 3D finite difference time domain simulations.

■ EXPERIMENTAL METHODS

Titanium Nitride (TiN) Film Deposition. Thin films of TiN with a $Cr_{90}Ru_{10}$ buffer layer were deposited by reactive DC magnetron sputtering from a 99.95% pure Ti target and $Cr_{90}Ru_{10}$ alloy target in an atmosphere of Ar and N_2 onto 3 in. fused silica or silicon substrates. The seed layer thickness is chosen to be 25 nm to avoid substrate-based oxidization through the diffusion of oxygen in fused silica.[40,41] In most cases, the TiN thickness was 50 nm, and that of the $Cr_{90}Ru_{10}$ seed was 25 nm, except for films intended for ATR studies where the thicknesses were necessarily reduced. Process parameters were deposition rates, controlled by magnetron power, the partial pressures of Ar and N_2 mediated through mass flow rates, and substrate temperature. The base pressure was 5×10^{-9} Torr and typical process pressure provided by an Ar flow rate of 5 sccm corresponded to 0.75×10^{-4} Torr. Optimal flow rates for N_2 were between 0.8 and 1 sccm and an estimated partial pressure of 0.9×10^{-4} Torr for 1 sccm N_2 and 0.8×10^{-4} Torr for 0.8 sccm N_2. Substrate temperature was independently calibrated by using a thermocouple attached to a test wafer. Deposition rate calibrations, film thickness measurements, and structural characterization were carried out using XRR and XRD on a Bruker D8 Discover X-ray diffractometer.

Crystallite size of thin TiN films was determined by using the Debye−Scherrer equation. $D = \frac{0.9\lambda}{\beta \cos \theta}$, where λ is the wavelength of the X-rays, β is the full width at half maximum of the peak, and θ is the diffraction angle at which the peak is located. Please note that we have not found any existence of the (200) peak at room temperature with no buffer configuration.

Optical Characterization. The films were characterized optically and plasmonically by ellipsometry and ATR measurements. Optical properties, expressed as dielectric permittivity (ϵ' and ϵ''), refractive index, and reflectivity, were obtained via a J.A. Woollam M-2000 ellipsometer. Thickness measured via XRR was introduced into the ellipsometry B-Spline model while maintaining the Kramers−Kronig relation.[32]

ATR measurements were done in the Kretschmann−Raether configuration, $\theta - 2\theta$, which is widely utilized for its precision in probing surface plasmon behavior. P-polarized (TM) light was obtained using a half-wave plate with a wavelength of 1550 nm was used to excite the SPP at the film/air interface through the substrate using a fused silica equilateral prism placed against the substrate and matched optically using a suitable index-matching fluid (n_{prism} = 1.444). The angle of incidence was swept through the critical angle of the prism, with a step size of 0.05° to allow evanescent coupling into the SPP resulting in a minimum in reflectance. The internal angle of incidence within a prism was calculated using Snell's law to correct it for the light refraction. The power of the incident laser was meticulously adjusted to ensure that neither the thin metallic sample nor the detectors were overwhelmed by the high incident light power (>100 μ W).[42,43]

Nanostructure Fabrication and CL Studies. The fabrication of TiN nanostructures was carried out by focused ion beam (FIB) (LYRA3 FIB−SEM, Tescan) on a 50 nm TiN film with 25 nm $Cr_{90}Ru_{10}$ seed layer deposited on a Si substrate at 300 °C. Si was needed for CL experiments as it does not emit in the spectral range of 450−850 nm and is sufficiently conductive to prevent the electron beam charging effect. The dielectric function of TiN on top of the Si substrate at 1.0 sccm condition at a substrate temperature of 300 °C is plotted in Supporting Information (Figure S1). The nanostructures were milled in the TiN layer by using a high-energy gallium ion beam. The beam energy and the ion beam current were kept at 30 keV and 30 pA, respectively.

CL experiments (shown in Figure S2) were conducted on an FEI Quanta 250 FEG scanning electron microscope in the high vacuum mode. The CL data were collected in the hyperspectral imaging mode where each pixel of the image contains a full set of spectral information during the scan over the region of interest.[44] An electron beam of 30 keV energy (current ∼6.6 nA) is incident onto the sample, and emitted photons caused by the interaction of electron energy and the particle's plasmon mode are directed to the cooled EMCCD with 1600 channels and 16 μm pixel pitch through the light collection path (in order): reflecting objective; fused silica vacuum window; off-axis parabolic mirror; and spectrograph as shown in Figure S2 (1/8 m spectrograph with 400 L/mm grating blazed at 500 nm and centered at 450 nm). However, none of these should have a pronounced feature in the range of 480−700 nm. The sample was mounted on the SEM sample holder and tilted 10° toward the CL collector for maximum light collection.[44]

COMSOL Multiphysics. The TM polarization-based reflectance properties of TiN thin films were calculated using a commercial finite element full wave solver (COMSOL Multiphysics).[45] The electromagnetic wave propagation is governed by Maxwell's wave equation in the frequency domain.

https://doi.org/10.1021/acsaelm.3c01344
ACS Appl. Electron. Mater. 2023, 5, 6929−6937

An active port boundary condition was used on the top side to simulate the incident light whereas a passive port was used at the bottom to minimize any artifact caused by the reflection in the computational domain. Floquet boundary conditions were also imposed on other boundaries to enable the symmetry of the electric field. The wavelength-dependent dielectric constants for TiN and $Cr_{90}Ru_{10}$ were taken from ellipsometry measurements. Those measurements fully agree with the analytical calculations of the TiN response and further validate the numerical analysis and support the experimental results as evident in Figure S3.

FDTD Simulations. Commercially available 3D finite-difference time-domain (FDTD) numerical simulations, specifically Ansys FDTD, were employed for the 3D-FDTD simulations. In FDTD, the Maxwell's equations are solved in the discretized space and time domains using the Yee algorithm.[46] The electron beam was modeled as a series of closely spaced dipoles having a phase difference related with the electron velocity. The current density is given by:

$$J(t, \vec{r}) = -ev\hat{u}_z\delta(z - vt)\delta(x - x_0)\delta(y - y_0) \quad (1)$$

where e and v represent the electron charge and the velocity of the electron (v = 0.32c corresponding to 30 keV electron energy), respectively. The electron beam is moving down along z (unit vector is denoted as $\hat{u}_z$) direction and initial coordinate of the e-beam was set at (x_0, y_0). The phase factor is defined as (z/v). The edge length and the thickness of the modeled triangular nanostructure were set as 1000 and 50 nm, respectively. The material property of the TiN (on a Si substrate) was defined by the refractive index information measured by ellipsometry (shown in Figure S1). We have calculated the Poynting vector components along the normal direction (P_z) at a large distance away from the sample in the upper hemisphere.

The Si substrate was set to have a refractive index of 4,[47,48] with a dimension of 5 μm × 5 μm × 2 μm. A mesh override region (3 nm × 3 nm × 2 nm) all over the TiN nanostructure along with the auto nonuniform meshing having mesh accuracy of 3 were used to calculate the CL response accurately. A very detailed description about the CL response from TiN nanoparticles can be found elsewhere.[47,48]

RESULTS AND DISCUSSION

Table 1 shows the deposition conditions of 50 nm films on top of a 25 nm $Cr_{90}Ru_{10}$ buffer layer on fused silica wafers (cross-sectional TEM image as shown in Figure S4). Figure 1 shows the permittivities of the films. It is very clear from both Figure 1a,b that the real part of permittivity shows more metallic behavior with increasing temperature for both partial pressures. Moreover, the optical losses are reduced significantly with elevated substrate temperatures as shown in Figure 1a,b. Although the trend is common for both partial pressures, the relative change in the optical losses in TiN thin films at different wafer/substrate temperatures is more prominent with a lower nitrogen partial pressure.

Table 1. Deposition Conditions of all the TiN Thin Films Studied Here

sample	substrate temperature in °C	partial pressure (Torr)
A_1	room temperature (RT)	0.8×10^{-4} (P_1)
A_2	RT	0.9×10^{-4} (P_2)
B_1	150	0.8×10^{-4} (P_1)
B_2	150	0.9×10^{-4} (P_2)
C_1	225	0.8×10^{-4} (P_1)
C_2	225	0.9×10^{-4} (P_2)
D_1	300	0.8×10^{-4} (P_1)
D_2	300	0.9×10^{-4} (P_2)

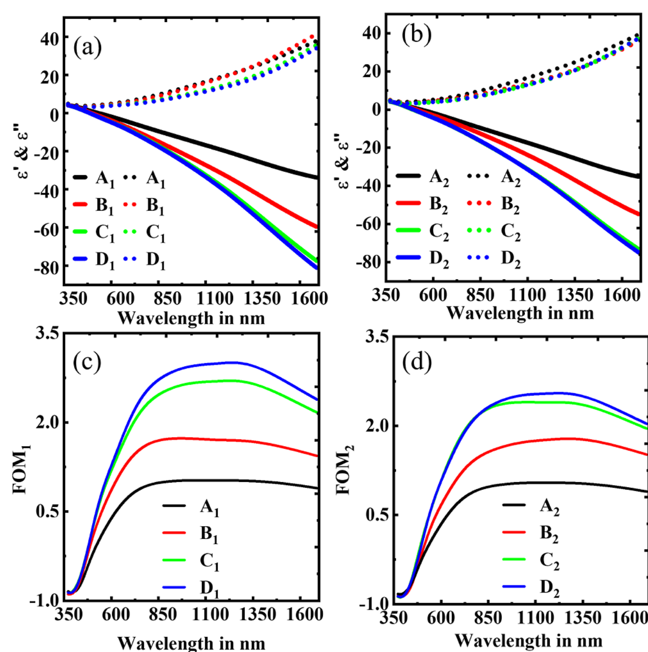

Figure 1. Dielectric constants of the different TiN thin film samples with $Cr_{90}Ru_{10}$ buffer layer deposited at (a) P_1 and (b) P_2. The solid lines in both (a,b) represent the real part of the dielectric function while dotted lines represent the imaginary part. (c,d) show respective FOMs.

Figure 1c,d represents the FOM of the TiN samples. It is clear from both the figures that the samples C_1, D_1, C_2, and D_2 are superior to any of those deposited below 150 °C (A_1, B_1, A_2, and B_2) for both partial pressures. The FOM reaches a maximum at 2.8 for the D_1 sample, whereas C_1, C_2, and D_2 reach around 2.65. It is worth noting that the films C_1, D_1, C_2, and D_2 show comparable FOM numbers to those films deposited at very high substrate temperature (above 500 °C) using reactive DC magnetron sputtering.[11,17,49,50]

After optimization, we have found that changes in both the real and imaginary parts were very marginal for the samples C_1, D_1, C_2, and D_2.

To gain a deeper insight into the enhancements shown in Figure 1, we compared the dielectric functions of the samples with and without buffer (NB) along with the RT results in Figure 2. It is very clear from Figure 2a that sample D_1 has the best optical properties compared to the high temperature/NB TiN thin film at the same temperature (D_1^{NB}) and the film deposited at RT (A_1). The trend is also consistent for sample D_2, grown at the higher rate of N_2 flow (1.0 sccm) as shown in Figure 2b. Their respective FOMs are shown in Figure 2, where FOM (c) is P_1 and FOM (d) is P_2. The optical properties of all deposited samples at different temperatures and partial pressures are shown in Supporting Information, Figure S5.

The dielectric functions of D_1 thin film have been compared with those from prior studies (as shown in Figure 3a,b), using similar methodology but different deposition conditions as shown in Table 2 below.[2,14,32,49,51]

Although Smith et al.[51] have reported that the use of a sapphire substrate may lead to a better response, with a substrate temperature in the range of 300−400 °C. This method also suffers from the poor cost-effectiveness of the sapphire substrate. It is also important to note that our results

https://doi.org/10.1021/acsaelm.3c01344
ACS Appl. Electron. Mater. 2023, 5, 6929−6937

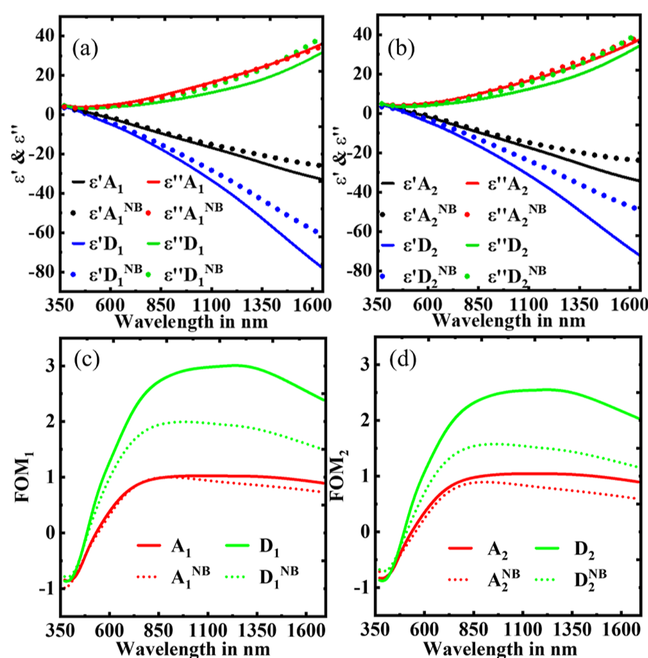

Figure 2. Comparison of dielectric function between TiN thin films with a buffer and no buffer (NB) layer deposited at RT and high temperatures at both P_1 and P_2. (a) A_1 and D_1 and (b) A_2 and D_2 and their respective FOMs (c) for figure (a) and (d) for figure (b).

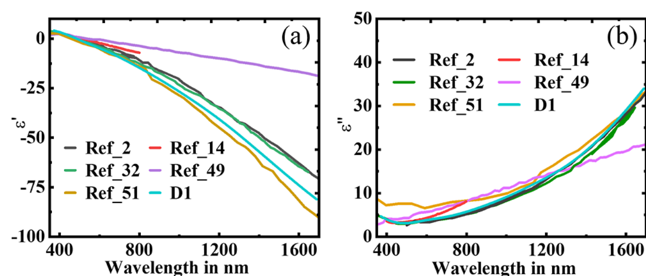

Figure 3. Comparison of (a) real and (b) imaginary parts of sample D_1 with respect to the other published studies. Reproduced with permission from refs 2 and 51. Copyright 2021 John Wiley and Sons and Copyright 2018 American Vacuum Society, respectively.

Table 2. Reference Sample Summary

references	substrate	interlayer	temperature (°C)
2	Al_2O_3(0001)	N/A	400
14	Al_2O_3	N/A	250
32	Si(001)	MgO	450
49	Al_2O_3	N/A	800
51	Al_2O_3(0001)	N/A	400

offer improved optical responses compared to the results reported by Ding et al.,[32] where the TiN was fabricated using MgO as the buffer layer. The use of a MgO layer may improve the lossy characteristic of the TiN thin film (as shown in Figure 3b) due to better lattice matching.[24] It also suffers additional oxidization[32] and poor cost-effectiveness in industrial processes. As discussed earlier, the utilization of $Cr_{90}Ru_{10}$ on amorphous substrates plays a crucial role in the deposition of plasmonically active TiN.

The $\theta-2\theta$ XRD pattern plots for all of the deposited films are shown in Figure 4. The presence of the buffer layer initiates the growth of TiN thin films in the preferred (200) direction,

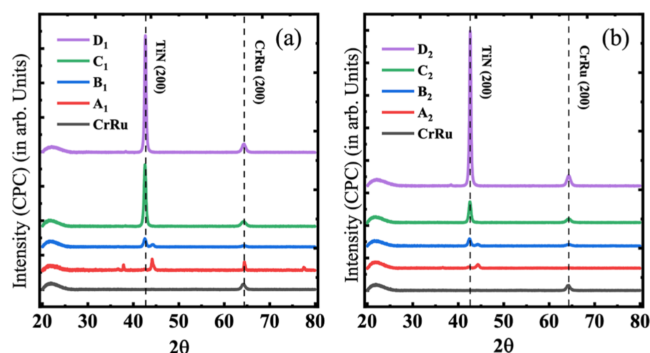

Figure 4. XRD scans of TiN samples deposited at (a) 0.8×10^{-4} (P_1 Torr) and (b) 0.9×10^{-4} Torr (P_2 Torr).

predominantly at ∼42.5°.[52,53] The monotonically increasing peak intensity with increasing substrate temperature, shown in Figure 4a,b (for both P_1 and P_2, respectively), suggests a homogeneous/uniform and textured fabrication of TiN thin films. Interestingly, the growth of TiN along the plane having least surface energy, that is (200), also suggests the formation of TiN films with fewer film defects and growth strain.[54] The $Cr_{90}Ru_{10}$ (200) peak is indexed around ∼64°.[39] The presence of smaller peaks around the central TiN peak can be attributed to the formation of oxide. In comparison with the XRD plots of TiN thin films with NB layer conditions (Figure S6), we have observed that the presence of $Cr_{90}Ru_{10}$ buffer layers plays an important role in the preferential growth of all TiN thin films along (200) direction. However, it is very clear from the X-ray analysis that the deposited TiN films are nonepitaxial[16] but highly textured[11] in nature.

Table 3 shows the comparison of crystallite size/grain size of TiN thin films with and without a buffer layer. It is noticed that

Table 3. Crystallite Size of TiN Thin Films[a]

	substrate temperature in °C			
grain sizes in nm	RT	150	225	300
grain size at P_1 with buffer/NB	17.5/–	15.7/14.4	19.0/16.8	22.7/17.0
grain size at P_2 with buffer/NB	18.4/–	14.5/12.9	17.4/15.7	23.0/19.9

[a] As shown in the XRD graphs with NB layer in Figure S6, the intensity of the (200) is very low; thus, the Debye Scherrer evaluation is not possible.

the higher temperature depositions in the presence of the $Cr_{90}Ru_{10}$ buffer layer not only initiate the preferential textured growth along (200) but also lead to the formation of TiN films having larger crystallite size/grain size, which can be attributed to the improvement of the loss function in the films, reducing carrier scattering.[16,55]

High-temperature deposition is always favorable for better thin film growth as it contributes toward minimizing the structural defects.[11,51,56] This trend is consistent with our present study as shown in Figures 1 and 2. Both of the responses in the real and imaginary parts are significantly improved in the presence of a buffer layer, characterized by lower real and imaginary parts of the dielectric permittivity. The $Cr_{90}Ru_{10}$ has a cubic lattice structure along the [200] direction (Figure S7), that plays an important role in improving the optical response of the TiN thin films by minimizing the lattice mismatch factor[17,32,50,51] along with

https://doi.org/10.1021/acsaelm.3c01344
ACS Appl. Electron. Mater. 2023, 5, 6929–6937

maintaining the cube-on-cube growth factor.[23,32] The improvement in the optical losses can be attributed in different ways: either the buffer layer of $Cr_{90}Ru_{10}$ improves the crystallinity[32] or the compressive strain of the TiN film[51,57,58] on $Cr_{90}Ru_{10}$ plays a crucial role at different substrate temperatures or both. Utilizing a buffer layer could offer advantages in creating plasmonically active TiN films with enhanced metallic behavior.

Titanium Nitride Annealing Studies. To qualify as a potential material for thermoplasmonic applications, thermal robustness must be assessed. To this end, anneals were carried out on thin film sample C_1, deposited at 225 °C and at P_1. Samples were annealed in the range of 300−600 °C with 100 °C increments in atmospheric and vacuum conditions. Figure 5a,b shows the change in optical response for (C_1) before and after various vacuum anneals. Both the real and imaginary parts of the dielectric function are improved with higher temperature annealing in vacuum. In addition, the screened plasma frequency (zero crossover) shows a prominent blue-shift trend with increasing temperature due to the bigger crystalline size, as well as enhanced TiN crystallinity.[52,59] It is also worth mentioning that the change in both the optical responses follows a monotonous trend except the 500 °C result, which might be attributed as an anomalous factor/artifact. Atmospheric anneals of TiN are shown in Figure 5c,d. The real part of the TiN shows a very stable response even under atmospheric conditions. Interestingly, the imaginary part shows a more lossy trend with increasing annealing temperature, which is likely due to the growth of the oxide layer as shown in Table S1. Due to the damage caused by the atmospheric annealing at very high temperatures alongside the 300−400 °C anneals, here it is not possible to fit to the ellipsometry data.

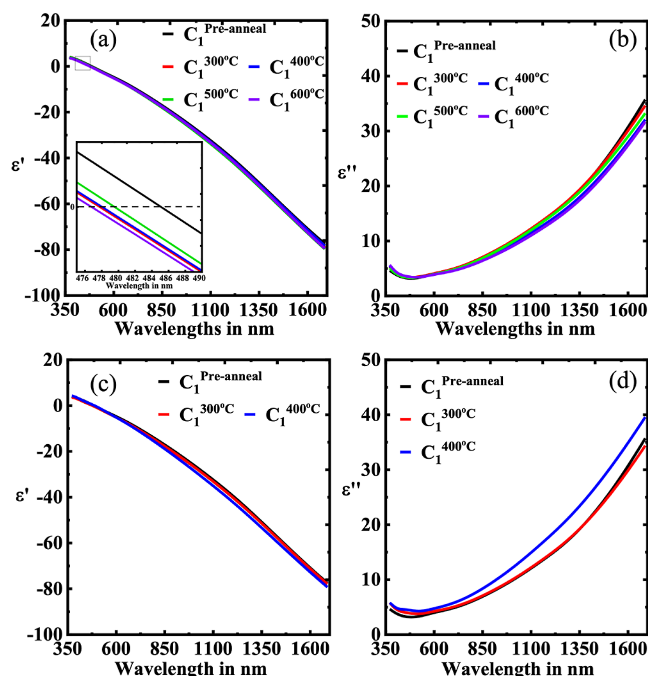

Figure 5. TiN anneal study results. (a,b) Dielectric responses at various temperatures under (a,b) vacuum and (c,d) atmospheric conditions.

This study shows that the sputtered film is capable of enduring temperatures as high as 600 °C under vacuum conditions. This attribute holds significant potential for various high-temperature applications, including solar thermophotovoltaics[60] and HAMR,[61] which could have wide-ranging implications.

Surface Plasmon-Assisted Optical Properties. *Attenuated Total Reflectance.* This experiment has been performed in Kretschmann configuration, and it is being used to probe the SPR capabilities of the TiN thin films. The incoming light needs to be evanescently coupled through optically lossy $Cr_{90}Ru_{10}$ to reach the TiN thin film as shown in Figure 6. In this configuration, a compromise has to be made between the thickness of the buffer layer and the thickness of the TiN to achieve the best results possible. The experimental ATR setup in Kretschmann configuration is shown in Figure S9.

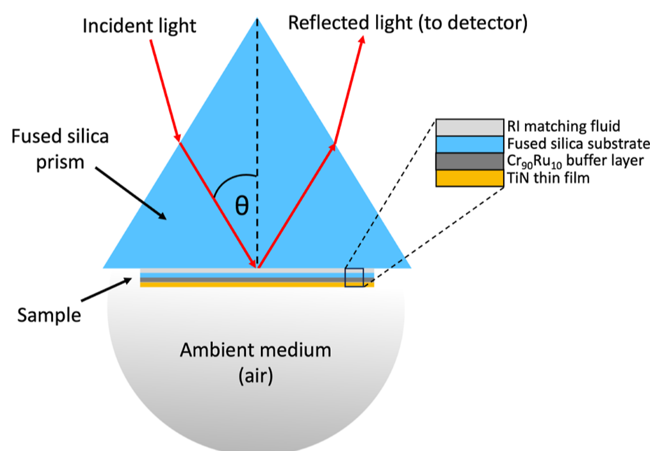

Figure 6. Schematic of the optical coupling setup in the Kretschmann configuration.

Before performing the experiments, the optimum coupling thickness was theoretically calculated using a multilayer reflection model for stratified media for the highest surface plasmon resonance efficiency.[62−64]

It was found that the optimal thickness for both the TiN samples C_1 and D_2 was 18 at 1550 nm wavelength. The dip in the reflectance spectra, shown in Figure 7a, relates to the excitation of SPPs at the TiN/air interface.[43,65] The calculated reflectance spectrum is in good agreement with the experimental responses as shown in Figure 7a. The broadening

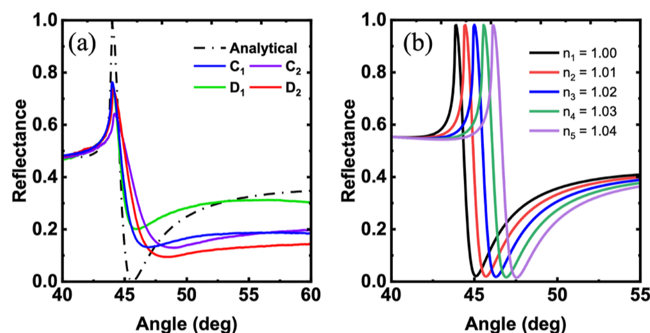

Figure 7. (a) Experimental ATR results of the TiN samples with a buffer layer compared to the analytical data. (b) Analytical ATR results showing the sensitivity of the TiN film to changes in the refractive index of the ambient medium.

https://doi.org/10.1021/acsaelm.3c01344
ACS Appl. Electron. Mater. 2023, 5, 6929−6937

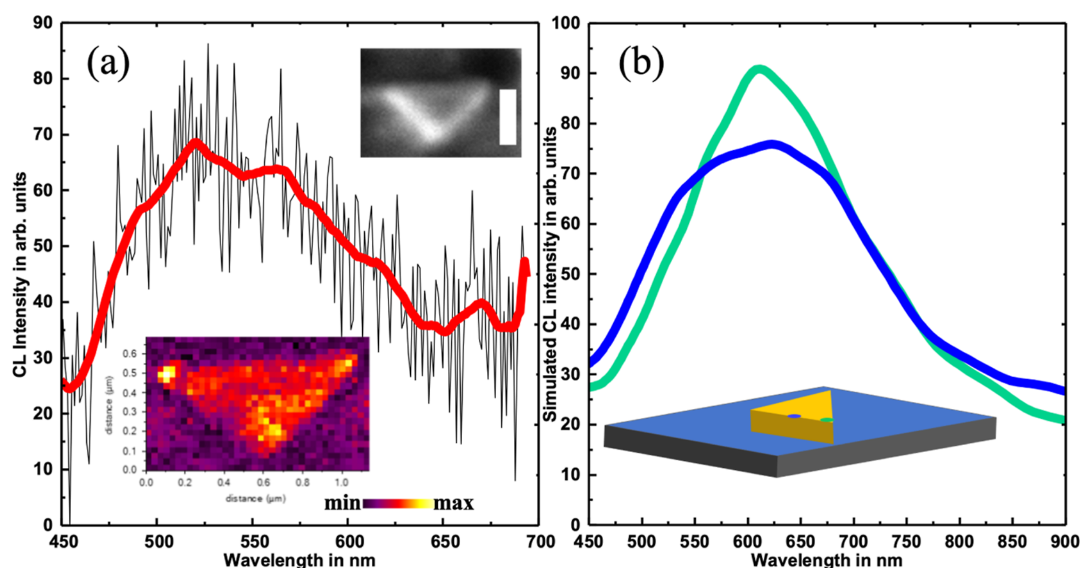

Figure 8. (a) Experimental CL response from triangular nanoparticle. (b) Simulated CL spectra from nanoparticle in the presence of the substrate. The CL spectra were calculated by placing the e-beam at two different locations over the nanoparticle (represented with different colors). The scale bar of the inset SEM image is 500 nm.

in all the spectra is very common and it can be attributed to the low carrier mobility (electrons) due to the larger absorptivity of TiN films than conventional plasmonic materials such as Au and Ag.[66] A slight mismatch between the calculated and experimentally acquired spectra can be understood as follows: a 2 nm seed layer of $Cr_{90}Ru_{10}$ is used to fabricate TiN thin films suitable for reflectance measurements. As $Cr_{90}Ru_{10}$ is optically absorptive, it may cause such a discrepancy and distort some of the coupling capabilities of TiN. In addition, many factors like temperature, humidity, build up of hydrocarbons on the metal surface, and so forth may have a role during the experimental measurements which cannot be accounted for in the calculated spectrum.

In order to explore the plasmonic behavior of the TiN thin film for sensing purposes, we calculate the reflectance by changing the refractive index of the ambient medium as shown in Figure 7b. In addition, the sensitivity value for the TiN sample curves has been calculated using the following equation:

$$S = \frac{\Delta\theta}{\Delta n} \tag{2}$$

The sensitivity of TiN, denoted as S_{TiN}, has been determined to be approximately 60 theta RIU^{-1}. This indicates that TiN exhibits high sensitivity suitable for sensing applications. Even minute changes in the refractive index of the external or ambient medium (whether it is metal or dielectric) can lead to substantial variations in the coupling angle, making TiN an excellent choice for sensing applications.[67,68]

CL Analyses. The CL response was recorded in the hyperspectral imaging mode. Furthermore, CL spectra were extracted using principal component analysis (PCA) based on the nonlinear iterative partial least-squares (NIPALS) method as described briefly elsewhere.[69] The calculated scree plot based on the aforementioned technique (shown in Figure S10) suggests the existence of a single PCA component. The first eigenspectrum and the corresponding CL image are shown in Figure 8a. A secondary electron image is also shown in the inset of Figure 8a. It is clear from the CL map (in Figure 8a) that photon emission is very prominent, particularly from the apex regions due to the strong electromagnetic coupling between the incident electron beam and the particle's plasmon mode.[70] It is also interesting to note that photon emission is comparatively much less prominent along the edges (particularly the edge on the right side of the image) of the triangular nanoparticle. The surface plasmon resonance is centered around a wavelength of 580 nm. 3D-FDTD simulations were carried out to explore the LSP response in a more detail way. We have modeled the nanotriangle having the edge length of 1000 nm and being placed on a Si substrate. The details of the numerical calculations are given in the method section. The calculated results shown in Figure 8b show very good agreement with the experimentally acquired CL results.

The CL responses were calculated by placing the electron beam at two different places over the modeled nanotriangular particle: at the tip position (tip-excitation) and at middle of the edge (edge-excitation). Figure 8b shows that the plasmon mode associated with the tip-excitation and the edge-excitation is centered around ∼600 and ∼630 nm, respectively. The intensity of the tip excitation is 25% stronger than that of edge-mode excitation. This suggests that there is efficient coupling of the plasmon modes at these apex regions. The spectral mismatch between experimental and simulated data can be attributed to the imperfect modeling of the nanotriangle object in terms of morphological details, including surface roughness,[71] radius of curvature of the apexes, and so forth. A broadening of ∼200 nm is common in both the experimental and the simulated CL results. Such broadening in CL response from bigger metal particles mainly arises due to the radiation losses.[27,67,72,73] The oscillation nature of the individual plasmon modes are masked due to the huge broadening in their spectral response compared to the distance between two resonance wavelengths (∼30 nm).[70] The photon emission or the surface plasmon excitation (shown in Figure 8a) is not related to any pure type of higher order mode of oscillations as the particle is bigger in size (retarded regime). The nature of the surface plasmon response might be the first-harmonic plasmon mode,[72] mixed,[73] hybridized, or substrate-modified in

https://doi.org/10.1021/acsaelm.3c01344
ACS Appl. Electron. Mater. 2023, 5, 6929−6937

nature.[74] In addition, the presence of the "hotspot" (where the electromagnetic local density of state is relatively high) at the apex regions has great importance particularly in heat-assisted-based modern nanophotonic technologies, like HAMR,[75−78] cancer therapy,[8,79] photothermal imaging, and so forth.[20,80] Moreover, the difference in the intensity of the electron-induced photon emission from different apexes caused by the tilted position of the sample stage is also providing a hint of the directionality of the photon emission.[69]

DISCUSSION/CONCLUSIONS

In summary, we have investigated the role of the $Cr_{90}Ru_{10}$ buffer layer in improving the optical properties of a titanium nitride thin film deposited on top of a fused silica substrate. We showed that process-dependent parametrization in terms of substrate temperature and the nitrogen gas flow rate also plays an important role in achieving better metallic quality and lower loss. The postdeposition annealing studies revealed the mechanical/thermal stability of the TiN thin films under vacuum conditions.

Reflectance studies employing the Kretschmann−Raether (K−R) configuration confirmed the successful excitation of SPPs at the air/TiN interface. Simulated reflectance studies, incorporating different refractive indices, highlighted the potential of TiN thin films for surface plasmon-assisted sensing applications. Hyperspectral CL studies, along with simulations, unveiled localized surface plasmon resonances in isolated TiN nanotriangle fabricated using FIB milling. In conclusion, our approach to achieving metallic TiN with minimal loss on industrially relevant substrates, even at substrate temperatures below 300 °C, presents a promising avenue for various plasmonic and metamaterial applications.

ASSOCIATED CONTENT

Supporting Information

The Supporting Information is available free of charge at https://pubs.acs.org/doi/10.1021/acsaelm.3c01344.

Dielectric function of TiN on the Si substrate; schematic of CL; experimental vs theoretical analysis of SPR curves; TEM−EDX of TiN thin films; dielectric functions of all deposited TiN thin films; XRD of TiN thin films with NB; XRD plot of $Cr_{90}Ru_{10}$; oxidization effect after annealing studies; experimental setup of ATR; and scree plot of eigenvalues (PDF)

AUTHOR INFORMATION

Corresponding Authors

Achyut Maity − *School of Mathematics and Physics, Queen's University Belfast, Belfast BT7 1NN, U.K.*; orcid.org/0000-0002-0562-7131; a.maity@qub.ac.uk

Robert M. Bowman − *School of Mathematics and Physics, Queen's University Belfast, Belfast BT7 1NN, U.K.*; Email: r.m.bowman@qub.ac.uk

Authors

Arthur F. Lipinski − *School of Mathematics and Physics, Queen's University Belfast, Belfast BT7 1NN, U.K.*; orcid.org/0000-0002-6580-3619

Christopher W. Lambert − *School of Mathematics and Physics, Queen's University Belfast, Belfast BT7 1NN, U.K.*

William R. Hendren − *School of Mathematics and Physics, Queen's University Belfast, Belfast BT7 1NN, U.K.*

Paul R. Edwards − *Department of Physics, SUPA, University of Strathclyde, Glasgow G4 0NG, U.K.*; orcid.org/0000-0001-7671-7698

Robert W. Martin − *Department of Physics, SUPA, University of Strathclyde, Glasgow G4 0NG, U.K.*; orcid.org/0000-0002-6119-764X

Complete contact information is available at: https://pubs.acs.org/10.1021/acsaelm.3c01344

Author Contributions

[§]A.F.L., C.W.L., and A.M. have contributed equally.

Notes

The authors declare no competing financial interest.

ACKNOWLEDGMENTS

The authors would like to acknowledge Dr. Sarah Ruddell from Queen's University Belfast and Mr. Tiernan McCaughery from Seagate Technology, Springtown for their help depositing thin films and TEM imaging, respectively. We acknowledge the support of Seagate Technology (Ireland) under SOW #00077300.0 and support by the Royal Academy of Engineering under the Research Chairs and Senior Research Fellowships Scheme along with funding from the Engineering and Physical Sciences Research Council (EPSRC) under grant number EP/S023321/1 and UKRI Strength in Places Fund programme Smart Nano NI.

REFERENCES

(1) Guler, U.; Boltasseva, A.; Shalaev, V. M. Refractory Plasmonics. *Science* **2014**, *344*, 263−264.

(2) Krekeler, T.; Rout, S. S.; Krishnamurthy, G. V.; Störmer, M.; Arya, M.; Ganguly, A.; Sutherland, D. S.; Bozhevolnyi, S. I.; Ritter, M.; Pedersen, K.; Petrov, A. Y.; Eich, M.; Chirumamilla, M. Unprecedented thermal stability of plasmonic titanium nitride films up to 1400 °C. *Adv. Opt. Mater.* **2021**, *9*, 2100323.

(3) Yu, M.-J.; Chang, C.-L.; Lan, H.-Y.; Chiao, Z.-Y.; Chen, Y.-C.; Howard Lee, H. W.; Chang, Y.-C.; Chang, S.-W.; Tanaka, T.; Tung, V.; Chou, H.-H.; Lu, Y.-J. Plasmon-enhanced solar-driven hydrogen evolution using titanium nitride metasurface broadband absorbers. *ACS Photonics* **2021**, *8*, 3125−3132.

(4) Chirumamilla, M.; Chirumamilla, A.; Yang, Y.; Roberts, A. S.; Kristensen, P. K.; Chaudhuri, K.; Boltasseva, A.; Sutherland, D. S.; Bozhevolnyi, S. I.; Pedersen, K. Large-area ultrabroadband absorber for solar thermophotovoltaics based on 3D titanium nitride nanopillars. *Adv. Opt. Mater.* **2017**, *5*, 1700552.

(5) Liu, Z.; Liu, G.; Huang, Z.; Liu, X.; Fu, G. Ultra-broadband perfect solar absorber by an ultra-thin refractory titanium nitride meta-surface. *Sol. Energy Mater. Sol. Cells* **2018**, *179*, 346−352.

(6) Ishii, S.; Sugavaneshwar, R. P.; Nagao, T. Titanium nitride nanoparticles as plasmonic solar heat transducers. *J. Phys. Chem. C* **2016**, *120*, 2343−2348.

(7) Bower, R.; Loch, D. A.; Ware, E.; Berenov, A.; Zou, B.; Hovsepian, P. E.; Ehiasarian, A. P.; Petrov, P. K. Complementary metal−oxide−semiconductor compatible deposition of nanoscale transition-metal nitride thin films for plasmonic applications. *ACS Appl. Mater. Interfaces* **2020**, *12*, 45444−45452.

(8) He, W.; Ai, K.; Jiang, C.; Li, Y.; Song, X.; Lu, L. Plasmonic titanium nitride nanoparticles for in vivo photoacoustic tomography imaging and photothermal cancer therapy. *Biomaterials* **2017**, *132*, 37−47.

(9) Shao, J.; Zhang, J.; Jiang, C.; Lin, J.; Huang, P. Biodegradable titanium nitride mxene quantum dots for cancer phototheranostics in NIR-I/II biowindows. *Chem. Eng. J.* **2020**, *400*, 126009.

(10) Guler, U.; Kildishev, A. V.; Boltasseva, A.; Shalaev, V. M. Plasmonics on the slope of enlightenment: the role of transition metal nitrides. *Faraday Discuss.* **2015**, *178*, 71−86.

(11) Naik, G. V.; Schroeder, J. L.; Ni, X.; Kildishev, A. V.; Sands, T. D.; Boltasseva, A. Titanium nitride as a plasmonic material for visible and near-infrared wavelengths. *Opt. Mater. Express* **2012**, *2*, 478−489.

(12) Naik, G. V.; Saha, B.; Liu, J.; Saber, S. M.; Stach, E. A.; Irudayaraj, J. M.; Sands, T. D.; Shalaev, V. M.; Boltasseva, A. Epitaxial superlattices with titanium nitride as a plasmonic component for optical hyperbolic metamaterials. *Proc. Natl. Acad. Sci. U.S.A.* **2014**, *111*, 7546−7551.

(13) Catellani, A.; Calzolari, A. Plasmonic properties of refractory titanium nitride. *Phys. Rev. B* **2017**, *95*, 115145.

(14) Kamakura, R.; Murai, S.; Ishii, S.; Nagao, T.; Fujita, K.; Tanaka, K. Plasmonic-photonic hybrid modes excited on a titanium nitride nanoparticle array in the visible region. *ACS Photonics* **2017**, *4*, 815−822.

(15) Guler, U.; Ndukaife, J. C.; Naik, G. V.; Nnanna, A. G. A.; Kildishev, A. V.; Shalaev, V. M.; Boltasseva, A. Local heating with lithographically fabricated plasmonic titanium nitride nanoparticles. *Nano Lett.* **2013**, *13*, 6078−6083.

(16) Sugavaneshwar, R. P.; Ishii, S.; Dao, T. D.; Ohi, A.; Nabatame, T.; Nagao, T. Fabrication of highly metallic TiN films by pulsed laser deposition method for plasmonic applications. *ACS Photonics* **2018**, *5*, 814−819.

(17) Shah, D.; Reddy, H.; Kinsey, N.; Shalaev, V. M.; Boltasseva, A. Optical properties of plasmonic ultrathin TiN films. *Adv. Opt. Mater.* **2017**, *5*, 1700065.

(18) Guo, W.-P.; Mishra, R.; Cheng, C.-W.; Wu, B.-H.; Chen, L.-J.; Lin, M.-T.; Gwo, S. Titanium nitride epitaxial films as a plasmonic material platform: alternative to gold. *ACS Photonics* **2019**, *6*, 1848−1854.

(19) M A, J.; Kolla, L. G.; Gnvr, V.; Nk, U.; Mohan, S. Pulsed DC magnetron sputtered titanium nitride thin films for localized heating applications in MEMS devices. *Sens. Actuators, A* **2018**, *272*, 199−205.

(20) Reddy, H.; Guler, U.; Kudyshev, Z.; Kildishev, A. V.; Shalaev, V. M.; Boltasseva, A. Temperature-dependent optical properties of plasmonic titanium nitride thin films. *ACS Photonics* **2017**, *4*, 1413−1420.

(21) Briggs, J. A.; Naik, G. V.; Petach, T. A.; Baum, B. K.; Goldhaber-Gordon, D.; Dionne, J. A. Fully CMOS-compatible titanium nitride nanoantennas. *Appl. Phys. Lett.* **2016**, *108*, 051110.

(22) Fomra, D.; Secondo, R.; Ding, K.; Avrutin, V.; Izyumskaya, N.; Özgür, Ü.; Kinsey, N. Plasmonic titanium nitride via atomic layer deposition: a low-temperature route. *J. Appl. Phys.* **2020**, *127*, 103101.

(23) Narayan, J.; Tiwari, P.; Chen, X.; Singh, J.; Chowdhury, R.; Zheleva, T. Epitaxial growth of TiN films on (100) silicon substrates by laser physical vapor deposition. *Appl. Phys. Lett.* **1992**, *61*, 1290−1292.

(24) Maurya, K. C.; Shalaev, V. M.; Boltasseva, A.; Saha, B. Reduced optical losses in refractory plasmonic titanium nitride thin films deposited with molecular beam epitaxy. *Opt. Mater. Express* **2020**, *10*, 2679−2692.

(25) Krylov, I.; Xu, X.; Qi, Y.; Weinfeld, K.; Korchnoy, V.; Eizenberg, M.; Ritter, D. Effect of the substrate on structure and properties of titanium nitride films grown by plasma enhanced atomic layer deposition. *J. Vac. Sci. Technol., A* **2019**, *37*, 060905.

(26) Murai, S.; Fujita, K.; Daido, Y.; Yasuhara, R.; Kamakura, R.; Tanaka, K. Plasmonic arrays of titanium nitride nanoparticles fabricated from epitaxial thin films. *Opt. Express* **2016**, *24*, 1143−1153.

(27) Gadalla, M. N.; Greenspon, A. S.; Tamagnone, M.; Capasso, F.; Hu, E. L. Excitation of strong localized surface plasmon resonances in highly metallic titanium nitride nano-antennas for stable performance at elevated temperatures. *ACS Appl. Nano Mater.* **2019**, *2*, 3444−3452.

(28) Saha, S.; Dutta, A.; Kinsey, N.; Kildishev, A. V.; Shalaev, V. M.; Boltasseva, A. On-chip hybrid photonic-plasmonic waveguides with ultrathin titanium nitride films. *ACS Photonics* **2018**, *5*, 4423−4431.

(29) Zhang, R.; Li, X.; Meng, F.; Bi, J.; Zhang, S.; Peng, S.; Sun, J.; Wang, X.; Wu, L.; Duan, J.; Cao, H.; Zhang, Q.; Gu, L.; Huang, L.-F.; Cao, Y. Wafer-scale epitaxy of flexible nitride films with superior plasmonic and superconducting performance. *ACS Appl. Mater. Interfaces* **2021**, *13*, 60182−60191.

(30) Gila, B.; Kim, J.; Luo, B.; Onstine, A.; Johnson, W.; Ren, F.; Abernathy, C.; Pearton, S. Advantages and limitations of MgO as a dielectric for GaN. *Solid-State Electron.* **2003**, *47*, 2139−2142.

(31) Izyumskaya, N.; Fomra, D.; Ding, K.; Morkoç, H.; Kinsey, N.; Özgür, Ü.; Avrutin, V. High-quality plasmonic materials TiN and ZnO: Al by atomic layer deposition. *Phys. Status Solidi RRL* **2021**, *15*, 2100227.

(32) Ding, K.; Fomra, D.; Kvit, A. V.; Morkoç, H.; Kinsey, N.; Özgür, Ü.; Avrutin, V. A platform for complementary metal-oxide-semiconductor compatible plasmonics: high plasmonic quality titanium nitride thin films on Si (001) with a MgO interlayer. *Adv. Photonics Res.* **2021**, *2*, 2000210.

(33) Frost, G.; Ladani, L. Development of high-temperature-resistant seed layer for electrodeposition of copper for microelectronic applications. *J. Electron. Mater.* **2020**, *49*, 1387−1395.

(34) Kim, Y.-J.; Lee, W.-B.; Choi, K.-K. Effect of seed layers and rapid thermal annealing on the temperature coefficient of resistance of NiCr thin films. *Thin Solid Films* **2019**, *675*, 96−102.

(35) Gu, Y.; Harada, H.; Ro, Y. Chromium and chromium-based alloys: problems and possibilities for high-temperature service. *JOM* **2004**, *56*, 28−33.

(36) Meng, B.; Tang, W.; Wang, Z.; Zhang, H. An optimized fabrication of high yield CMOS-compatible silicon carbide capacitive pressure sensors. *2012 7th IEEE International Conference on Nano/Micro Engineered and Molecular Systems (NEMS)*, 2012; pp 721−724.

(37) Gill, A. A.; Ghoreishizadeh, S. S. Advances in nanomaterials integration in CMOS-based electrochemical sensors: a review. *IEEE Sensor. J.* **2023**, *23*, 4659−4671.

(38) Perez, M. R.; Mejia, I.; Salas-Villasenor, A. L.; Stiegler, H.; Trachtenberg, I.; Gnade, B. E.; Quevedo-Lopez, M. A. Hybrid CMOS thin-film devices based on solution-processed CdS n-TFTs and TIPS-Pentacene p-TFTs. *Org. Electron.* **2012**, *13*, 3045−3049.

(39) Dong, K.; Li, H.; Hu, J.; Peng, Y.; Ju, G.; Chow, G.; Chen, J. Control of microstructure and magnetic properties of FePt films with TiN intermediate layer. *IEEE Trans. Magn.* **2013**, *49*, 668−674.

(40) Williams, E. Diffusion of oxygen in fused silica. *J. Am. Ceram. Soc.* **1965**, *48*, 190−194.

(41) He, H.; Yu, J. Effect of adsorbed water on mechanical and mechanochemical properties of silicate glasses. *J. Non-Cryst. Solids: X* **2023**, *18*, 100189.

(42) Paliwal, A.; Sharma, A.; Tomar, M.; Gupta, V. Room temperature detection of NO_2 gas using optical sensor based on surface plasmon resonance technique. *Sens. Actuators, B* **2015**, *216*, 497−503.

(43) Mukhtar, W. M.; Halim, R. M.; Hassan, H. Optimization of SPR signals: Monitoring the physical structures and refractive indices of prisms. *EPJ Web of Conferences*, 2017; p 01001.

(44) Edwards, P. R.; Jagadamma, L. K.; Bruckbauer, J.; Liu, C.; Shields, P.; Allsopp, D.; Wang, T.; Martin, R. W. High-resolution cathodoluminescence hyperspectral imaging of nitride nanostructures. *Microsc. Microanal.* **2012**, *18*, 1212−1219.

(45) Yushanov, S.; Gritter, L.; Crompton, J.; Koppenhoefer, K. Surface Plasmon Resonance. *COMSOL Conference*, 2012.

(46) Sullivan, D. M. *Electromagnetic Simulation Using the FDTD Method*; John Wiley & Sons, 2013.

(47) Maity, A.; Maiti, A.; Das, P.; Senapati, D.; Kumar Chini, T. Effect of intertip coupling on the plasmonic behavior of individual multitipped gold nanoflower. *ACS Photonics* **2014**, *1*, 1290−1297.

(48) Maity, A.; Maiti, A.; Satpati, B.; Patsha, A.; Dhara, S.; Chini, T. K. Probing localized surface plasmons of trisoctahedral gold nanocrystals for surface enhanced raman scattering. *J. Phys. Chem. C* **2016**, *120*, 27003−27012.

(49) Naik, G. V.; Kim, J.; Boltasseva, A. Oxides and nitrides as alternative plasmonic materials in the optical range [Invited]. *Opt. Mater. Express* **2011**, *1*, 1090−1099.
(50) Zgrabik, C. M.; Hu, E. L. Optimization of sputtered titanium nitride as a tunable metal for plasmonic applications. *Opt. Mater. Express* **2015**, *5*, 2786−2797.
(51) Smith, H. A.; Elhamri, S.; Eyink, K. G.; Grazulis, L.; Hill, M. J.; Back, T. C.; Urbas, A. M.; Howe, B. M.; Reed, A. N. Epitaxial titanium nitride on sapphire: effects of substrate temperature on microstructure and optical properties. *J. Vac. Sci. Technol., A* **2018**, *36*, 03E107.
(52) Yu, I.-S.; Cheng, H.-E.; Chang, C.-C.; Lin, Y.-W.; Chen, H.-T.; Wang, Y.-C.; Yang, Z.-P. Substrate-insensitive atomic layer deposition of plasmonic titanium nitride films. *Opt. Mater. Express* **2017**, *7*, 777−784.
(53) Chang, C.-C.; Nogan, J.; Yang, Z.-P.; Kort-Kamp, W. J.; Ross, W.; Luk, T. S.; Dalvit, D. A.; Azad, A. K.; Chen, H.-T. Highly plasmonic titanium nitride by room-temperature sputtering. *Sci. Rep.* **2019**, *9*, 15287−15289.
(54) Gu, P.; Zhu, X.; Li, J.; Wu, H.; Sun, H.; Yang, D. Influence of substrates on the properties of titanium nitride films deposited by DC reaction magnetron sputtering. *Appl. Phys. A: Mater. Sci. Process.* **2018**, *124*, 550−559.
(55) Patsalas, P.; Kalfagiannis, N.; Kassavetis, S. Optical properties and plasmonic performance of titanium nitride. *Materials* **2015**, *8*, 3128−3154.
(56) Yang, Z.-Y.; Chen, Y.-H.; Liao, B.-H.; Chen, K.-P. Room temperature fabrication of titanium nitride thin films as plasmonic materials by high-power impulse magnetron sputtering. *Opt. Mater. Express* **2016**, *6*, 540−551.
(57) Bi, J.; Zhang, R.; Peng, S.; Sun, J.; Wang, X.; Chen, W.; Wu, L.; Gao, J.; Cao, H.; Cao, Y. Robust plasmonic properties of epitaxial TiN films on highly lattice-mismatched complex oxides. *Phys. Rev. Mater.* **2021**, *5*, 075201.
(58) Shah, D.; Catellani, A.; Reddy, H.; Kinsey, N.; Shalaev, V.; Boltasseva, A.; Calzolari, A. Controlling the plasmonic properties of ultrathin tin films at the atomic level. *ACS Photonics* **2018**, *5*, 2816−2824.
(59) Wang, Y.; Capretti, A.; Dal Negro, L. Wide tuning of the optical and structural properties of alternative plasmonic materials. *Opt. Mater. Express* **2015**, *5*, 2415−2430.
(60) Wang, H.; Chen, Q.; Wen, L.; Song, S.; Hu, X.; Xu, G. Titanium-nitride-based integrated plasmonic absorber/emitter for solar thermophotovoltaic application. *Photonics Res.* **2015**, *3*, 329−334.
(61) Mehta, V. V., Reiner, J. W., Salo, M. P., Wood, R. W. Heat-assisted magnetic recording (HAMR) disk drive with disk having multiple continuous magnetic recording layers. U.S. Patent 9,601,144 B1, 2017.
(62) Vigoureux, J. M. Polynomial Formulation of Reflection and Transmission by Stratified Planar Structures. *J. Opt. Soc. Am. A* **1991**, *8*, 1697.
(63) Chen, N. C.; Lien, W. C.; Liu, C. R.; Huang, Y. L.; Lin, Y. R.; Chou, C.; Chang, S. Y.; Ho, C. W. Excitation of surface plasma wave at tin/air Interface in the Kretschmann geometry. *J. Appl. Phys.* **2011**, *109*, 043104−043107.
(64) Du, C.; Liu, L.; Ma, S.; Liu, Z.; Zhu, J.; He, Y.; Wang, Z.; Guo, J. Experimental study of the optimal metal film for surface plasmon resonance. *Eighth International Conference on Photonics and Imaging in Biology and Medicine*, 2009; Vol. *7519*, p 75190J.
(65) Schasfoort, R. B. *Handbook of Surface Plasmon Resonance*; Royal Society of Chemistry, 2017.
(66) Asencios, J.; Moro, R.; Luyo, C.; Talledo, A. High sensitive biosensors based on the coupling between surface plasmon polaritons on titanium nitride and a planar waveguide mode. *Sensors* **2020**, *20*, 1784.
(67) Maier, S. A. *Plasmonics: Fundamentals and Applications*; Springer Science & Business Media, 2007.
(68) Homola, J.; Yee, S. S.; Gauglitz, G. Surface plasmon resonance sensors: review. *Sens. Actuators, B* **1999**, *54*, 3−15.
(69) Edwards, P. R.; Sleith, D.; Wark, A. W.; Martin, R. W. Mapping localized surface plasmons within silver nanocubes using cathodoluminescence hyperspectral imaging. *J. Phys. Chem. C* **2011**, *115*, 14031−14035.
(70) Myroshnychenko, V.; Nelayah, J.; Adamo, G.; Geuquet, N.; Rodríguez-Fernández, J.; Pastoriza-Santos, I.; MacDonald, K. F.; Henrard, L.; Liz-Marzán, L. M.; Zheludev, N. I.; Kociak, M.; García de Abajo, F. J. Plasmon spectroscopy and imaging of individual gold nanodecahedra: a combined optical microscopy, cathodoluminescence, and electron energy-loss spectroscopy Study. *Nano Lett.* **2012**, *12*, 4172−4180.
(71) Rodríguez-Fernández, J.; Funston, A. M.; Perez-Juste, J.; Alvarez-Puebla, R. A.; Liz-Marzán, L. M.; Mulvaney, P. The effect of surface roughness on the plasmonic response of individual sub-micron gold spheres. *Phys. Chem. Chem. Phys.* **2009**, *11*, 5909−5914.
(72) Askes, S. H.; Schilder, N. J.; Zoethout, E.; Polman, A.; Garnett, E. C. Tunable plasmonic HfN nanoparticles and arrays. *Nanoscale* **2019**, *11*, 20252−20260.
(73) Bower, R.; McPolin, C. P.; Krasavin, A. V.; Zayats, A. V.; Petrov, P. K. Temperature stability of individual plasmonic Au and TiN nanodiscs. *Opt. Mater. Express* **2022**, *12*, 3471−3479.
(74) Kawasaki, N.; Meuret, S.; Weil, R.; Lourenço-Martins, H.; Stéphan, O.; Kociak, M. Extinction and scattering properties of high-order surface plasmon modes in silver nanoparticles probed by combined spatially resolved electron energy loss spectroscopy and cathodoluminescence. *ACS Photonics* **2016**, *3*, 1654−1661.
(75) Challener, W. A.; Peng, C.; Itagi, A. V.; Karns, D.; Peng, W.; Peng, Y.; Yang, X.; Zhu, X.; Gokemeijer, N. J.; Hsia, Y. T.; Ju, G.; Rottmayer, R. E.; Seigler, M. A.; Gage, E. C. Heat-assisted magnetic recording by a near-field transducer with efficient optical energy transfer. *Nat. Photonics* **2009**, *3*, 220−224.
(76) Challener, W. A.; Itagi, A. V. *Modern Aspects of Electrochemistry No. 44*; Springer, 2009; pp 53−111.
(77) Gosciniak, J.; Mooney, M.; Gubbins, M.; Corbett, B. Novel droplet near-field transducer for heat-assisted magnetic recording. *Nanophotonics* **2015**, *4*, 503−510.
(78) Datta, A.; Xu, X. Improved near-field transducer design for heat-assisted magnetic recording. *IEEE Trans. Magn.* **2016**, *52*, 1−6.
(79) Huang, X.; Jain, P. K.; El-Sayed, I. H.; El-Sayed, M. A. Plasmonic photothermal therapy (PPTT) using gold nanoparticles. *Laser Med. Sci.* **2008**, *23*, 217−228.
(80) Guler, U.; Shalaev, V. M.; Boltasseva, A. Nanoparticle plasmonics: going practical with transition metal nitrides. *Mater. Today* **2015**, *18*, 227−237.

https://doi.org/10.1021/acsaelm.3c01344
ACS Appl. Electron. Mater. 2023, 5, 6929−6937